

# Three-dimensional Polymers as Organic Cathodes for Affordable and Sustainable Sodium/Potassium-ion Batteries

Motahareh Mohammadirooubbari,<sup>[a]</sup> Shi Li,<sup>[b]</sup> Jinghao Huang,<sup>[a]</sup> Zhenzhen Yang,<sup>[c]</sup> Fu Chen,<sup>[d]</sup> Lei Cheng,<sup>[e]</sup> and Chao Luo<sup>\*[a, f]</sup>

Redox-active polymers (RAPs) are promising organic electrode materials for affordable and sustainable batteries due to their flexible chemical structures and negligible solubility in the electrolyte. Developing high-dimensional RAPs with porous structures and crosslinkers can further improve their stability and redox capability by reducing the solubility and enhancing reaction kinetics. This work reports two three-dimensional (3D) RAPs as stable organic cathodes in Na-ion batteries (NIBs) and K-ion batteries (KIBs). Carbonyl functional groups are incorpo-

rated into the repeating units of the RAPs by the polycondensation of Tetrakis(4-aminophenyl)methane and two different dianhydrides. The RAPs with interconnected 3D extended conjugation structures undergo multi-electron redox reactions and exhibit high performance in both NIBs and KIBs in terms of long cycle life (up to 8000 cycles) and fast charging capability (up to  $2 \text{ A g}^{-1}$ ). The results demonstrate that developing 3D RAPs is an effective strategy to achieve high-performance, affordable, and sustainable NIBs and KIBs.

## Introduction

Lithium-ion batteries (LIBs) have dominated the energy storage market for consumer electronics, electric transportation, and grid-scale energy storage due to their high energy density and long cycle life.<sup>[1–5]</sup> However, lithium suffers from uneven geographical distribution and restricted supply chains, which not only enhance the battery manufacturing cost but also limit the large-scale applications.<sup>[6,7]</sup> Moreover, as the global community moves towards carbon neutrality by utilizing renewable energy sources, LIBs cannot meet the ever-increasing demand for high-performance, environmentally benign, and sustainable batteries.<sup>[8]</sup> The new design for sustainable grid-scale energy storage systems becomes more critical. To this end, sodium and

potassium with the advantages of low cost, abundance, high sustainability, and similar physicochemical properties to lithium are promising alternatives for developing next-generation affordable and sustainable batteries.<sup>[9–15]</sup>

The rocking chair mechanism in LIBs extends to Na-ion batteries (NIBs) and K-ion batteries (KIBs), but the larger sizes of  $\text{Na}^+/\text{K}^+$  compromise the performance of inorganic cathode materials.<sup>[16–18]</sup> Moreover, the inorganic compounds are mainly composed of heavy and toxic transition metals such as cobalt and nickel, increasing the cost, energy consumption, and environmental burden of NIB and KIB production.<sup>[19,20]</sup> Compared with the inorganic counterparts, organic electrode materials (OEMs) consisting of lightweight elements and flexible chemical structures offer numerous opportunities for material structure design and performance optimization of sustainable alkali-ion batteries.<sup>[21–26]</sup> The organic/polymeric synthetic pathways can be easily tailored to introduce various redox-active sites, conjugation structures, electron-withdrawing/donating functional groups, side chains, and crosslinkers in OEMs, tuning their conformation, structure isomerism, aromaticity, porosity, and physicochemical properties.<sup>[27]</sup> Though considerable research efforts have been devoted to developing advanced OEMs, the structure-performance correlations in organic NIBs and KIBs remain elusive. It is paramount to gain a fundamental understanding of these correlations to address the challenges of organic batteries such as low conductivity, high electrolyte solubility, and particle pulverization, achieving high-performance, affordable, and sustainable organic NIBs and KIBs.<sup>[28,29]</sup>

As well-documented, polymerization is a practical approach to suppressing the solubility of small organic molecules in organic electrolytes.<sup>[30–32]</sup> Redox-active polymers (RAPs) with flexible long chains, crosslinkers, and extended conjugation structures offer fast reaction kinetics and rapid electron transfer, resulting in superior cycling performance.<sup>[33–39]</sup> Among them,

[a] Dr. M. Mohammadirooubbari, J. Huang, Prof. C. Luo  
Department of Chemistry and Biochemistry, George Mason University,  
Fairfax, VA 22030, USA  
E-mail: cluo@gmu.edu

[b] Dr. S. Li  
Material Science Division, Argonne National Laboratory, Lemont, IL 60439,  
USA

[c] Dr. Z. Yang  
Chemical Sciences and Engineering Division, Argonne National Laboratory,  
Lemont, IL 60439, USA

[d] Dr. F. Chen  
Department of Chemistry and Biochemistry, University of Maryland, College Park, MD 20742, USA

[e] Dr. L. Cheng  
Chemical Sciences Division, Oak Ridge National Laboratory, Oak Ridge, TN 37831, USA

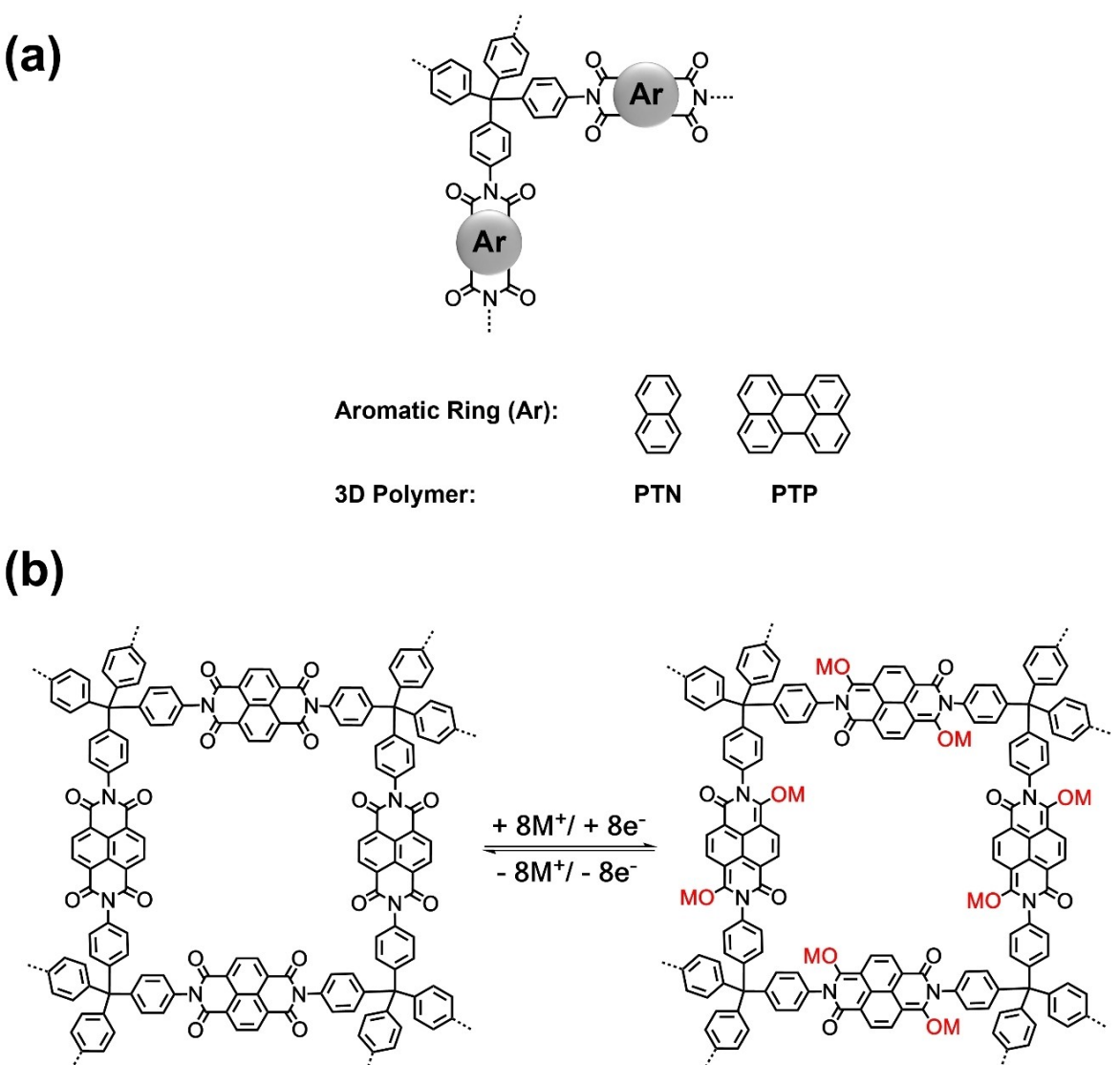
[f] Prof. C. Luo  
Quantum Science & Engineering Center, George Mason University, Fairfax, VA 22030, USA

 Supporting information for this article is available on the WWW under  
<https://doi.org/10.1002/batt.202300472>

carbonyl-based RAPs stand out because of their abundant structure diversity and flexible molecular tunability.<sup>[40–43]</sup> However, the formation of unstable free radical intermediates by the intramolecular electron transfer during the electrochemical reactions between carbonyl groups and ions/electrons hinders their cycle life.<sup>[44,45]</sup> To address this challenge, introducing extended conjugation structures, electron-withdrawing/donating functional groups, and side chains into RAPs stabilizes the reaction intermediates and products, leading to improved battery performance.<sup>[46,47]</sup> Moreover, Growing the polymeric chains in more than one direction to build two-dimensional (2D) organic frameworks is also an effective strategy for maintaining structural stability and reducing solubility.<sup>[48,49]</sup> In our previous work, we proved that 2D RAPs with various conjugation structures and porosity exhibit high capacity, high stability, and fast reaction kinetics in NIBs and KIBs, demonstrating great promise for developing high-performance sustainable batteries.<sup>[50]</sup> To further prolong the lifetime of RAPs, developing

three-dimensional (3D) RAPs with crosslinked, porous, and extended conjugation structures, as well as large surface area is critical.

In this work, two 3D polyimides with carbonyl functional groups are designed as cathodes for NIBs and KIBs. The monomer with four benzene rings and a  $\text{sp}^3$  carbon in the center enabled the 3D structure of the two polymers. The step-growth polymerization method allowed the growth of polymer chains in three dimensions to form a 3D network. The extended conjugation structure in polymers facilitates electron/ion transfer, leading to faster reaction kinetics and higher reversible capacity.<sup>[51]</sup> The chemical structures of two polymers named PTN and PTP are shown in Scheme 1(a). The presence of eight carbonyl groups in the repeating unit of these polymers enables multi-electron redox reactions. The proposed multi-electron redox reaction mechanism is displayed in Scheme 1(b). The carbonyl groups reversibly react with  $\text{Na}^+/\text{K}^+$ , accompanied by intramolecular electron transfer in conjugation structures.<sup>[52–54]</sup>



**Scheme 1.** Structures and reaction mechanism: a) the molecular structure of two 3D polymers; b) the proposed reaction mechanism for PTN as an example, where M represents Na/K ions.

The high solubility of organic electrode materials in the liquid electrolyte is a major challenge in organic batteries, leading to fast capacity loss upon cycling. To address this challenge, we leveraged the polymerization method to develop one-dimensional and two-dimensional polymers to reduce the solubility of organics in the electrolyte.<sup>[50,54]</sup> Herein, we developed three-dimensional (3D) polymers to introduce more crosslinked and extended conjugation structures in the polymers, further reducing the solubility in the electrolytes. The two 3D polymers, PTN and PTP, are insoluble in the 1 M NaPF<sub>6</sub>/KPF<sub>6</sub> in EC:PC electrolytes, resulting in high cyclic performance in NIBs and KIBs. Single-layer graphene was added to the composition of cathodes to enhance the conductivity and further restrain the solubility of active materials in the electrolyte.<sup>[55–57]</sup> The highly conductive graphene sheets can accommodate the large volume change of active materials during redox reactions by the  $\pi$ - $\pi$  stacking between the conjugation structures of graphene and PTN/PTP. The polymer-graphene cathodes exhibited exceptional electrochemical performances in both NIBs and KIBs. Though PTN delivered higher initial capacities in NIBs and KIBs, PTP with a larger delocalized  $\pi$ -conjugation structure showed more stable electrochemical performance. PTP with an interconnected 3D extended conjugation structure exhibits high performance in both NIBs and KIBs in terms of long cycle life (up to 8000 cycles) and fast charging capability (up to 2 A g<sup>-1</sup>). The results demonstrate that developing 3D polyimides with extended conjugation structures is a promising approach to achieving high-performance RAPs for affordable and sustainable batteries.

## Results and Discussion

The 3D polymers were synthesized by a reported one-pot condensation polymerization method using tetrakis(4-aminophenyl)methane (TAM) and naphthalenetetracarboxylic dianhydride (NTCDA)/Perylenetetracarboxylic dianhydride (PTCDA) as monomers.<sup>[58,59]</sup> Different characterization techniques such as X-ray diffraction (XRD), solid-state nuclear magnetic resonance (NMR), Fourier-transform infrared spectroscopy (FTIR), and scanning electron microscopy (SEM) were utilized to verify the chemical structures and morphology of the polymers. The XRD patterns of the polymers did not show any sharp peaks, but there were a couple of small and broad peaks around 11° and 25°, representing some orders along the chains of PTN. There were also two broad peaks around 16° and 24° related to small crystalline regions in PTP (Figure S1). To investigate the molecular structures of the synthesized polymers, solid-state <sup>13</sup>C NMR and <sup>17</sup>O NMR were employed since the 3D polymers were insoluble in organic solvents. As shown in Figure 1(a), the peak at 161.78 ppm is related to the carbonyl carbons in PTN. The phenyl carbons bonded with N were represented by the peak at 145.47 ppm, while the other phenyl carbons in the repeating unit of PTN were represented by the peak at 126.83 ppm.<sup>[60]</sup> The small peak at 47.24 ppm stands for the sp<sup>3</sup> carbon in the TAM moiety of PTN.<sup>[61,62]</sup> As shown in Figure 1(b), PTP also showed similar peaks at 162.16 and

145.26 ppm assigned to the carbonyl carbons and N-bonded phenyl carbons, respectively. The peaks corresponding to the other phenyl carbons in the repeating unit of PTP are located at 131.68 and 122.37 ppm. The peak at 51.30 ppm stands for the sp<sup>3</sup> carbon in the TAM moiety of PTP.<sup>[63]</sup> The other small peaks close to 50 ppm can be related to the spinning sidebands of aromatic carbons.<sup>[64]</sup> The <sup>17</sup>O NMR spectra showed peaks at 378.93 and 379.78 ppm, corresponding to the carbonyl oxygens for PTN and PPT, respectively (Figure 1c and d).<sup>[65]</sup> The FTIR spectra of the monomers and related polymers are shown in Figure 1(e and f). The characteristic peak for amine groups in the structure of TAM was not observed in the spectra of polymers. Instead, the peak corresponding to amide groups appeared around 1343 cm<sup>-1</sup> for PTN.<sup>[44]</sup> The peaks between 1580 and 1680 cm<sup>-1</sup> belonged to the symmetric and asymmetric stretching vibrations of carbonyl groups. They were shifted to lower wavenumbers after polymerization since introducing more aromatic rings and amide groups into the repeating units of PTN and PTP lowered the absorption energy.<sup>[59,66]</sup> The X-ray photoelectron spectroscopy (XPS) results, which were calibrated by the C–C peak in the C 1s spectrum at 284.8 eV (Figure S2), showed peaks corresponding to the C–C and C=O bonds.<sup>[67]</sup> In the O1s spectrum, the peak at 532.5 eV is assigned to the oxygen in the C=O group. In the N 1s spectrum, the peak at 400.3 eV is assigned to the C–N group (Figure S2). As shown in Figure 1(g and h), the polymers demonstrated different shapes of microparticles due to the structural variation in the repeating units of the polymers. Both PTN and PTP were identified as irregularly shaped microparticles dispersed in amorphous regions. Brunauer-Emmett-Teller (BET) surface area analysis was also conducted to measure the porosity and surface area of the 3D polymers. The PTN with a 3D interconnected framework shows a highly porous structure, where the average pore size and surface area are 2.1 nm and 352.12 m<sup>2</sup> g<sup>-1</sup>, respectively (Figure S3). The computational method was also employed to simulate the 3D structures of PTN and PTP. The dihedral angle scan performed on the interaction between DNI/PDI and benzene, as depicted in Figure S4, illustrates a vertical alignment between these molecular groups. The energy variation observed is restricted to less than 20 meV within a 90° ± 30° range, which is lower than the thermal energy. This implies a dynamic rotational behavior for the PTN and PTP within a 30° range at room temperature. Figures S5 and S6 display the optimized structure of the extensive polymer repeat unit as well as a single relaxed polymer chain with 10–15 repeating units as computed by GFN2-xTB. The dihedral angles for PTN (108.8° ± 7.5°) and PTP (114.75° ± 1.3°) are in good agreement with the corresponding values obtained from DFT calculations. The results from material characterizations confirmed the successful polymerization of PTN/PTP and provided insights into the chemical structure and morphology of the 3D polymers.

The electrochemical performances of PTN and PTP as cathodes in NIBs were evaluated by cyclic voltammetry (CV) and galvanostatic charge-discharge (GCD) tests. The polymers were tested in the cutoff window of 1–3.5 V to identify the redox plateaus and assess the cycling performance. 20 wt% of single-layer graphene was added to the cathodes to boost the

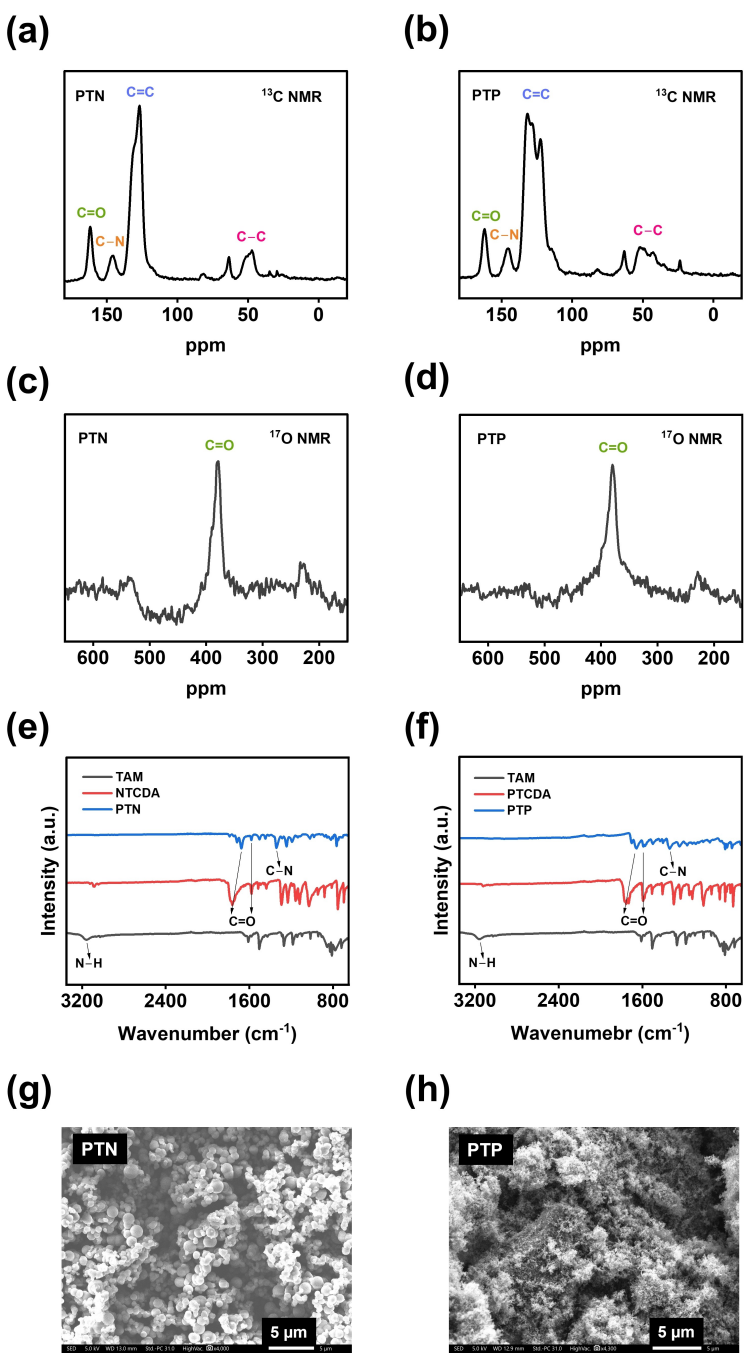


**Figure 1.** Material characterizations for PTN and PTP: a and b)  $^{13}\text{C}$  solid-state NMR, c and d)  $^{17}\text{O}$  solid-state NMR, e and f) FTIR spectra, g and h) SEM images.

conductivity and stability of polymeric cathodes. Carbonate-based electrolytes were prepared by making 1 M  $\text{NaPF}_6$  solution in two types of solvents, ethylene carbonate (EC): propylene carbonate (PC)/diethyl carbonate (DEC). The CV plots at the scan rate of 0.1  $\text{mVs}^{-1}$  revealed two pairs of sharp peaks for the PTN cathode at 1.8 and 2.2 V (Figure 2a). These cathodic and anodic peaks confirm the reversible redox reaction of carbonyl active sites with Na ions/electrons. As shown in Figure 2(b), the charge-discharge curves displayed two pairs of plateaus at 1.9 and 2.0 V during initial cycles, which are consistent with the redox peaks in the CV plot. The PTN cathode delivered an initial

charge capacity of 109.3  $\text{mAh g}^{-1}$  at the current density of 20  $\text{mA g}^{-1}$  (Figure 2b). The cell demonstrated stable cycling performance with a retention factor of ~84% after 100 cycles (Figure 2c). To explore the cyclability of the cells in NIBs, the specific capacity was recorded at different current densities. The charge capacity was maintained higher than 77  $\text{mAh g}^{-1}$  for 200 cycles at 50  $\text{mA g}^{-1}$  (Figure 2d). As shown in Figure 2(e), great cycling stability is demonstrated by the PTN cathode at the current density of 100  $\text{mA g}^{-1}$  for 300 cycles. Moreover, the rate capability was assessed in incremental current densities from 20  $\text{mA g}^{-1}$  to 2000  $\text{mA g}^{-1}$ . As shown in Figure 2(f), the

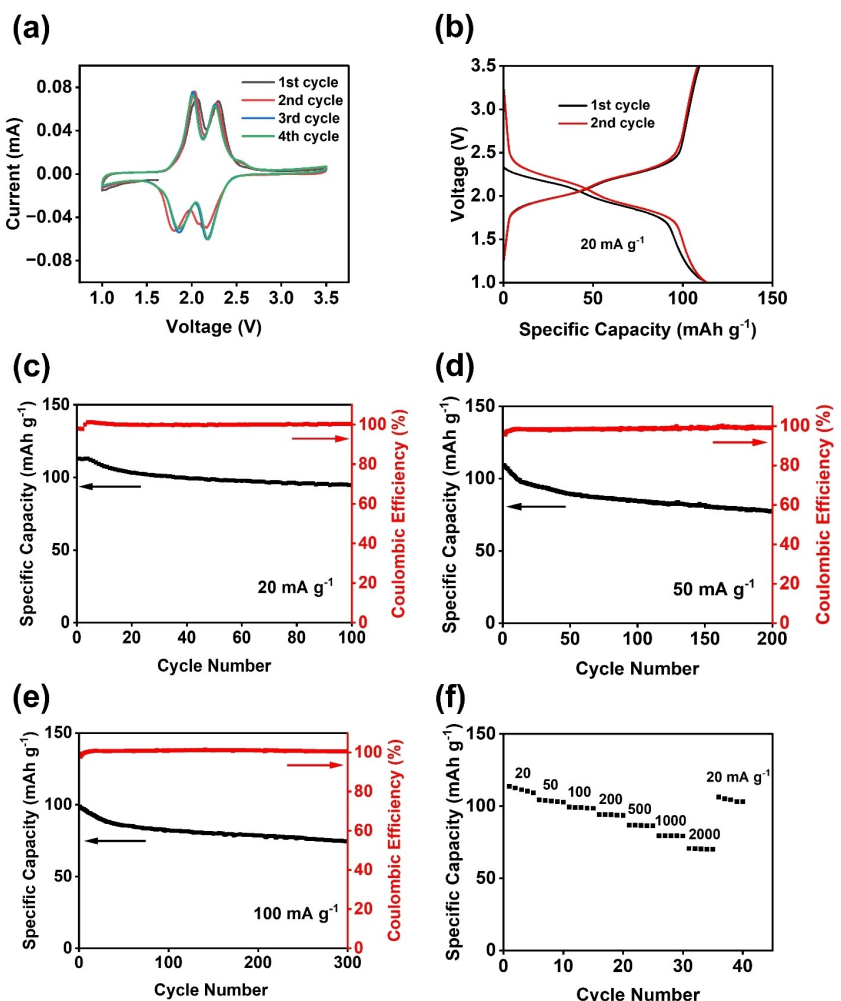


**Figure 2.** Electrochemical performance of PTN for NIBs in 1 M NaPF<sub>6</sub> in EC:PC (1:1 volume ratio): a) cyclic voltammograms at 0.1 mV s<sup>-1</sup>; b) galvanostatic charge-discharge curves at 20 mA g<sup>-1</sup>; de-sodiation capacity and Coulombic efficiency versus cycle number at the current density of c) 20 mA g<sup>-1</sup>, d) 50 mA g<sup>-1</sup>, e) 100 mA g<sup>-1</sup>; f) rate capability at various scan rates.

initial capacity delivered at 20 mA g<sup>-1</sup> was recovered by a high retention factor of 93% after being tested at 2000 mA g<sup>-1</sup>, suggesting robust reaction kinetics for the PTN cathode. PTN with a naphthalene backbone grown in a 3D structure showed a high electrochemical performance in NIBs. Selecting an electrolyte with high ionic conductivity and a wide electrochemical stability window also impacts stable cycling performance.<sup>[68,69]</sup> Carbonate-based electrolytes offering high ionic conductivity and stability at high voltages show great promise in NIBs and KIBs even at low concentrations.<sup>[70,71]</sup> The electrochemical performance of PTN with 1 M NaPF<sub>6</sub> in EC:DEC (1:1 volume ratio) as an electrolyte has also been provided in Figure S7. As expected, the PTN cathode showed very similar performances as those in 1 M NaPF<sub>6</sub> in EC:PC (1:1 volume ratio) electrolyte. The comparison between the polymeric cathodes fabricated with and without single-layer graphene is shown in Figure S8. The presence of graphene improves the conductivity of the polymer cathodes, resulting in higher specific capacities for both PTN and PTP cathodes.

To verify the fast reaction kinetics of PTN in NIBs, CV at various scan rates, galvanostatic intermittent titration technique (GITT), and electrochemical impedance spectroscopy (EIS) were carried out. The change in the voltage and current of cathodic and anodic peaks was monitored by the CV test at the scan rates of 0.1–1 mV s<sup>-1</sup> (Figure 3a). The potential hysteresis for cathodic and anodic peaks was increased at higher scan rates due to the larger polarization. As shown in Figure 3(b), the values for the slope of the fitted line are equal to 0.8691 and 0.9193 for cathodic and anodic peaks, respectively. These values were calculated using  $I = axv^b$  equation to determine if the redox reaction is leaning more towards surface-controlled or diffusion-controlled. Since the numbers are close to 1.0, the pseudo-capacitive behavior is dominant for the kinetics of the redox reaction. The GITT curves showed very low overpotentials during the charge and discharge plateaus, indicating that efficient ion transfer leads to fast and robust reaction kinetics. To investigate the ion transfer resistance in the electrolyte, at the interface of the cathode and the electrolyte, and inside the electrode, EIS was employed. This technique provides insights

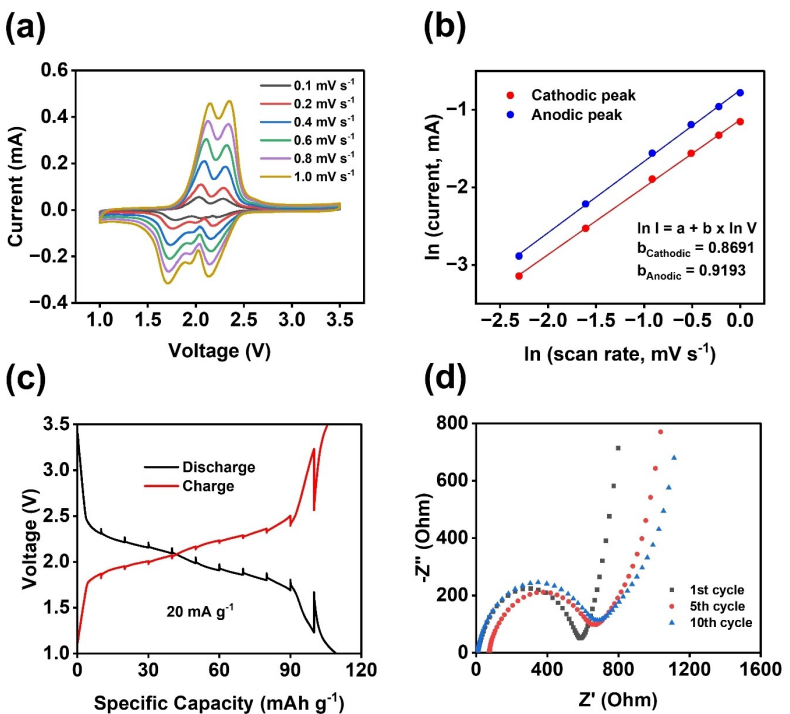


**Figure 3.** Reaction kinetics of PTN for NIBs in 1 M NaPF<sub>6</sub> in EC:PC (1:1 volume ratio): a) cyclic voltammograms at various scan rates; b) the natural logarithm of peak current versus scan rate; c) potential response during GITT measurements; d) impedance analysis after cycling.

into thermodynamics and kinetics by testing the cells at both low and high-frequency regions after cycling. As shown in Figure 3(d), the initial semi-circle representing the interfacial resistance did not show a significant increase after the 10<sup>th</sup> cycle. The slight increase in interfacial resistance and diffusion resistance resulted in some capacity decay as shown in the cycling performance. Overall, the results from CV, GITT, and EIS suggest PTN as a promising cathode with fast reaction kinetics in NIBs.

The electrochemical performance of PTP with the perylene moiety in the repeating units of the polymer was also evaluated in NIBs. To confirm the reversible redox reaction, a CV test was performed. The CV curves showed two close cathodic peaks at ~2.0 and 2.2 V related to the redox reaction at the carbonyl groups. The corresponding anodic peaks overlapped yielding one strong peak at ~2.2 V as shown in Figure 4(a). The charge-discharge curves for the PTP cathode at the current density of 20 mA g<sup>-1</sup> exhibited one pair of redox plateaus centered at 2.1 V, corresponding to the multi-electron redox reaction (Figure 4b). The similar redox peaks/plateaus overlap was also observed in other polyimides.<sup>[59,72]</sup> The initial reversible capacity of 94.7 mA h g<sup>-1</sup> was delivered by the PTP cathode. As shown in Figure 4(c), the specific capacity remained stable for 200 cycles with a high Coulombic efficiency of ~100%. Moreover, a capacity retention of 90% was preserved after 2,000 cycles at 100 mA g<sup>-1</sup> (Figure 4d). Since the PTP showed an excellent cycling performance, the fast-charging capability was evaluated at the high current density of 1,000 mA h g<sup>-1</sup>. As shown in Figure 4(e), the PTP cathode retained a remarkably stable cycling performance with a Coulombic efficiency of 100% for

8,000 cycles. This outstanding performance is very promising for fast-charging applications of organic cathodes in NIBs. The rate capability test was further conducted to confirm fast and robust reaction kinetics for the PTP cathode. The initial capacity was recovered by a retention factor of 97% at the current densities from 20 mA g<sup>-1</sup> to 2,000 mA g<sup>-1</sup> with minimal capacity decay at each increment (Figure 4f). The electrochemical performance of PTP with 1 M NaPF<sub>6</sub> in EC:DEC as the electrolyte has also been provided in Figure S9. Similarly, the PTP cathode showed a very stable cycling performance in this electrolyte. In Table S1, the summary of electrochemical performance confirms that our designed 3D polymers feature fast-charging capability with comparably high redox potentials in NIBs.<sup>[72-74]</sup>

The reaction kinetics for the PTP cathode in NIBs was studied by testing the CV at scan rates from 0.1–1.0 mV s<sup>-1</sup>. As shown in Figure 5(a), similar anodic and cathodic peaks were detected at higher scan rates with larger polarization. The calculated b values are equal to 0.9712 and 0.9760, confirming that pseudo-capacitive behavior controls the kinetics of the redox reaction (Figure 5b). The slope values for PTP are higher compared to PTN, indicating that the surface-controlled reaction plays a more significant role in the kinetics of the PTP cathode. In addition, the very low overpotential in the GITT curves is another indication of robust reaction kinetics for the PTP cathode in NIBs (Figure 5c). As shown in Figure 5(d), the depressed semi-circle assigned to the interfacial resistance was decreased from the 1<sup>st</sup> cycle to the 10<sup>th</sup> cycle. This confirms the formation of a stable cathode electrolyte interphase (CEI) after cycling, leading to an outstanding cycling performance. The interfacial resistance changes of PTN and PTP upon cycling are

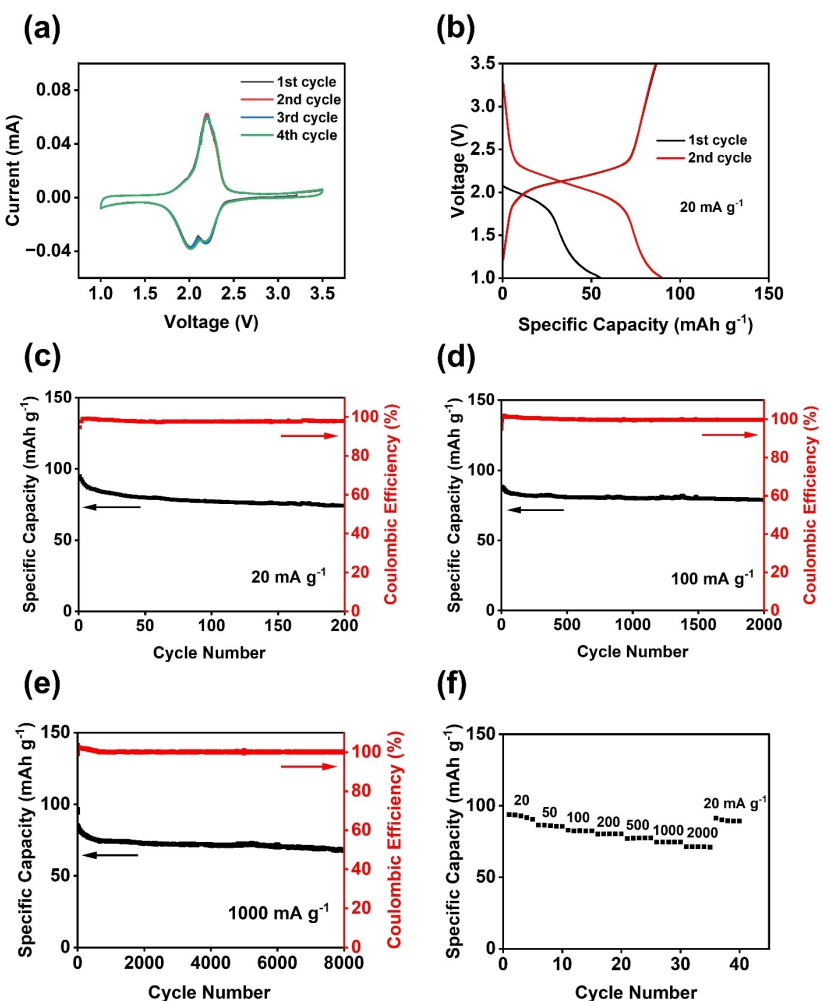


**Figure 4.** Electrochemical performance of PTP for NIBs in 1 M NaPF<sub>6</sub> in EC:PC (1:1 volume ratio): a) cyclic voltammograms at 0.1 mVs<sup>-1</sup>; b) galvanostatic charge-discharge curves at 20 mA g<sup>-1</sup>; de-sodiation capacity and Coulombic efficiency versus cycle number at the current density of c) 20 mA g<sup>-1</sup>, d) 100 mA g<sup>-1</sup>, e) 1000 mA g<sup>-1</sup>; f) rate capability at various scan rates.

different. The initial capacity of PTN is higher than that of PTP, indicating more Na-ion insertion/extraction and a larger volume change during charge and discharge. The large volume change damages the interphase of the PTN cathode and exposes a new PTN surface to the electrolyte, resulting in the continuous growth of the interphase between the PTN cathode and the electrolyte in the initial cycles. Since the depressed semi-circles represent the interfacial resistance between the cathode and the electrolyte, the damage and continuous growth of the interphase lead to the increase of the resistance of the PTN cathode. In addition, the initial capacity decay of PTN is faster than that of PTP, also contributing to the resistance increase of the PTN cathode. The PTP cathode with a larger conjugation structure offers a more stable cycling performance with lower resistance at the interphase between the cathode and the electrolyte. The collective results from cycling performance and reaction kinetics prove the fast and robust kinetics for the PTP cathode in NIBs. The perylene with a larger conjugated structure in PTP facilitates the intramolecular electron transfer,

resulting in a better electrochemical performance than that of PTN with a naphthalene backbone.

Since the polymers demonstrated great performance in NIBs, their electrochemical performances were also evaluated in KIBs at similar conditions. As shown in Figure 6(a), two cathodic peaks appeared at ~2.0 and ~2.3 V in the CV plot, suggesting a multi-electron redox reaction for the PTN cathode in KIBs. The redox reaction was reversible as indicated by the corresponding anodic peaks at ~2.3 and ~2.7 V. A reversible capacity of 134.9 mAh g<sup>-1</sup> was delivered by the cell tested in the cutoff window of 1–3.8 V at the current density of 20 mA g<sup>-1</sup> (Figure 6b). Two pairs of redox plateaus at ~2.2 and ~2.5 V were observed in the galvanostatic charge and discharge curves. The PTN cathode showed a stable cycling performance at 20 mA g<sup>-1</sup> for 100 cycles (Figure 6c). To further evaluate the cycle life of the PTN cathode in KIBs, it was measured at elevated current densities. As shown in Figure 6(d and e), initial capacities of 119.5 and 113.4 mAh g<sup>-1</sup> were delivered at 50 mA g<sup>-1</sup> and 100 mA g<sup>-1</sup>, respectively. The PTN cathode showed stable cyclic performance for 500 cycles. Though the larger size of potassium

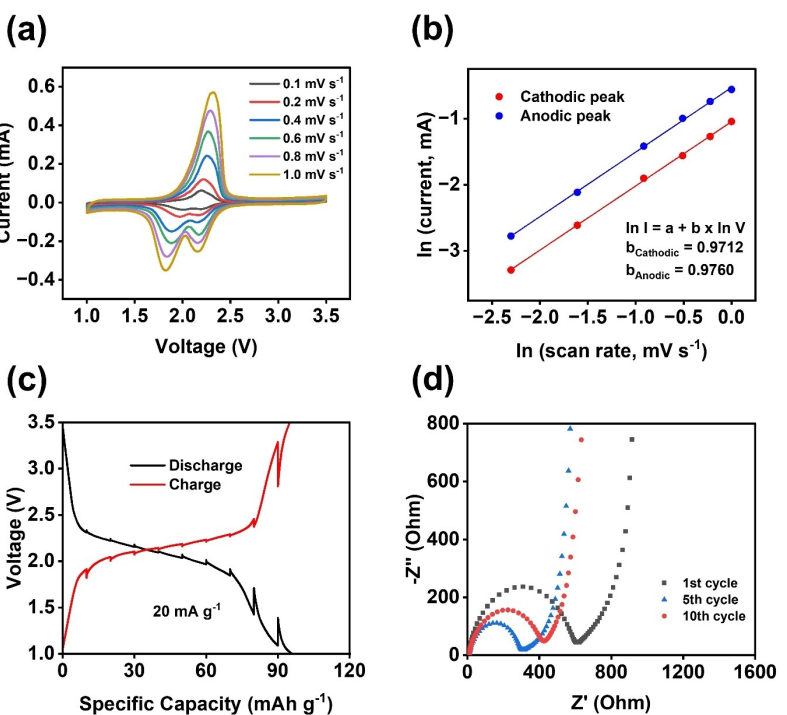


**Figure 5.** Reaction kinetics of PTP for NIBs in 1 M  $\text{NaPF}_6$  in EC:PC (1:1 volume ratio): a) cyclic voltammograms at various scan rates; b) the natural logarithm of peak current versus scan rate; c) potential response during GITT measurements; d) impedance analysis after cycling.

ions causes large volume expansion/shrinkage of the active material during battery charge/discharge, the 3D architecture of PTN accommodates those structural changes and minimizes capacity decay, demonstrating a high-performance polymer cathode in KIBs. In addition to the cycle life tests, the rate capability test was conducted at current densities from  $20 \text{ mA g}^{-1}$  to  $2000 \text{ mA g}^{-1}$  to analyze reaction kinetics. As shown in Figure 6(f), an average capacity of  $86.8 \text{ mAh g}^{-1}$  was retained at the high current density of  $2,000 \text{ mA g}^{-1}$ . Afterward, the PTN cathode recovered the initial average capacity at  $20 \text{ mA g}^{-1}$  with a retention factor higher than 90% immediately. The superb cycling performance and rate capability are significant for the application of the PTN cathode in KIBs.

Since the PTN cathode exhibited high performance in KIBs, the PTP cathode was also tested in KIBs. As shown in Figure 7(a), two cathodic peaks were observed at  $\sim 2.1$  and  $\sim 2.4$  V, representing the redox reaction of the carbonyl functional groups. The anodic peaks were merged, yielding a broad peak at  $\sim 2.6$  V. The charge-discharge curves of PTP showed one pair of sloping plateaus centered at  $\sim 2.4$  V (Figure 7b), consistent with the redox peaks in the cyclic voltammogram. The PTP cathode delivered an initial capacity of  $98.1 \text{ mAh g}^{-1}$  at the current density of  $20 \text{ mA g}^{-1}$ . The cell retained the capacity by a retention factor of 75% for 200 cycles as shown in Figure 7(c). Furthermore, the PTP cathode showed a very stable cycling performance at  $100 \text{ mA g}^{-1}$  with a Coulombic efficiency of 100% for 1,000 cycles (Figure 7d). To further exploit the fast-charging capability in KIBs, the PTP cathode was measured at the current density of  $1,000 \text{ mA g}^{-1}$ . As shown in Figure 7(e), the cell exhibited excellent capacity retention, preserving a capacity

higher than  $70 \text{ mAh g}^{-1}$  for 1000 cycles. This result is promising for the fast-charging application of organic cathodes in KIBs. The rate capability test at the incremental current density of  $20\text{--}2000 \text{ mA g}^{-1}$  demonstrated robust reaction kinetics. The cells showed minimal capacity decay when tested at higher current densities of up to  $2000 \text{ mA g}^{-1}$  (Figure 7f). Therefore, PTP featuring a 3D interconnected conjugation structure exhibited superior cyclic stability and fast-charging capability, demonstrating a promising polymer cathode material in KIBs. The performance comparison between PTN and PTP in NIBs/KIBs is shown in Figure S10.

To verify the proposed redox mechanism and investigate the CEI in the polymer cathode, XPS was utilized. XPS is a surface-sensitive technique, which explores the relative abundance of the elemental composition and chemical state of materials by measuring the binding energy of the elements. The PTN cathodes were monitored at different charge and discharge stages in NIBs to exploit the changes in different chemical compositions on the surface of electrodes. As shown in Figure 8, C 1s, O 1s, and F 1s spectra of the pristine electrodes, the cathode discharged to 1 V, and the cathode charged to 3.5 V are compared to understand the evolution of chemical structures during charge/discharge. For the carbon analyses, the reference peak of graphitic carbon was calibrated at 284.8 eV.<sup>[67,76]</sup> In C 1s spectra, the peak at 289.4 eV showed increased intensity after discharging to 1 V, indicating that the highly oxidized carbons were formed in the interphase layer. In the O 1s spectrum of the pristine cathode, the peak at 532.5 eV was assigned to the C=O group.<sup>[76]</sup> Another peak appeared at 533.5 eV after being discharged to 1 V, representing the C–O

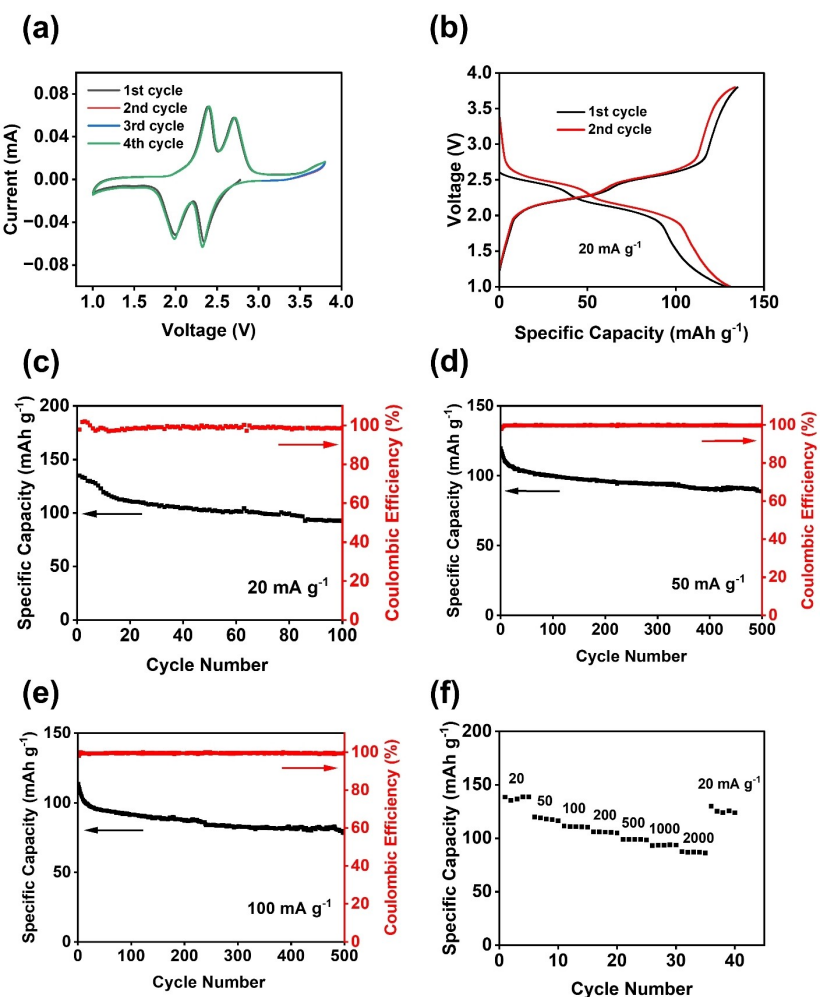


**Figure 6.** Electrochemical performance of PTN in KIBs: a) cyclic voltammograms at  $0.1 \text{ mV s}^{-1}$ ; b) galvanostatic charge-discharge curves at  $20 \text{ mA g}^{-1}$ ; De-potassiation capacity and Coulombic efficiency versus cycle number at the current density of c)  $20 \text{ mA g}^{-1}$ , d)  $50 \text{ mA g}^{-1}$ , e)  $100 \text{ mA g}^{-1}$ ; f) rate capability at various scan rates.

group formed after the reduction of the  $\text{C=O}$  group by Na ions and electrons. This peak was preserved with higher intensity at the fully charged stage, demonstrating the  $\text{C=O}$  group was also present in the CEI. In the F 1s spectrum of the pristine cathode, the peak at  $689.7 \text{ eV}$  was assigned to  $\text{C-F}$  corresponds to the polytetrafluoroethylene (PTFE) binder in the cathodes. After being discharged to  $1 \text{ V}$ , the peaks at  $686.8 \text{ eV}$  and  $684.3 \text{ eV}$  belonged to  $\text{P-F}$  and  $\text{NaF}$  groups from the CEI showed up.<sup>[77]</sup> The  $\text{P-F}$  and  $\text{NaF}$  peaks were retained after being fully charged to  $3.5 \text{ V}$ , confirming that they are formed in the CEI of the cathode. The formation of a  $\text{NaF}$ -rich CEI stabilizes the PTN cathode upon long-term cycling. The XPS spectra of PTN cathodes at different stages of potassiation/depotassiation in KIBs are shown in Figure S11. In the C 1s spectra, the peaks at  $284.8$ ,  $285.6$ ,  $286.4$ ,  $289.4$ , and  $292.5 \text{ eV}$  were assigned to  $\text{C-C}$ ,  $\text{C-O/C-N}$ ,  $\text{C=O}$ ,  $\text{O-C=O}$ , and  $\text{C-F}$  bonds, respectively. The pristine electrode did not exhibit any peaks related to the  $\text{K 2p}$  signals. However, the peak at  $\sim 296 \text{ eV}$  appeared after discharging to  $1 \text{ V}$ , corresponding to  $\text{K } 2\text{P}_{1/2}$  in the potassiated cathode. The peak at  $292.5 \text{ eV}$  showed increased intensity due to the overlap of  $\text{K } 2\text{P}_{3/2}$  and the  $\text{C-F}$  peaks.<sup>[78]</sup> In addition, the O 1s

and F 1s XPS spectra demonstrated similar changes as those observed in NIBs. The  $\text{C=O}$  peaks appeared at  $533.6 \text{ eV}$  after discharge/charge in KIBs. In F 1s spectra, the peak at  $684.4 \text{ eV}$  is assigned to  $\text{KF}$ , which is a critical component in the CEI. The XPS results confirmed that carbonyl functional groups are the redox-active sites in NIBs and KIBs, while the formation of  $\text{NaF}/\text{KF}$  species on the surface of the PTN cathode improves the stability of the CEI and cyclic stability.

Post-cycling characterizations such as SEM and FTIR were performed on the cycled PTN electrodes to investigate the changes in the morphology and chemical structure of the polymer cathode. The SEM images of the pristine PTN electrode and the electrodes cycled in NIBs were compared in Figure S12. No significant changes were observed in the shape or integrity of polymeric microparticles. Similarly, the FTIR spectra of the PTN cathode at different stages of cycling did not indicate any changes in the characteristic peaks (Figure S13), demonstrating the high structure integrity of the PTN cathode upon long-term cycling.

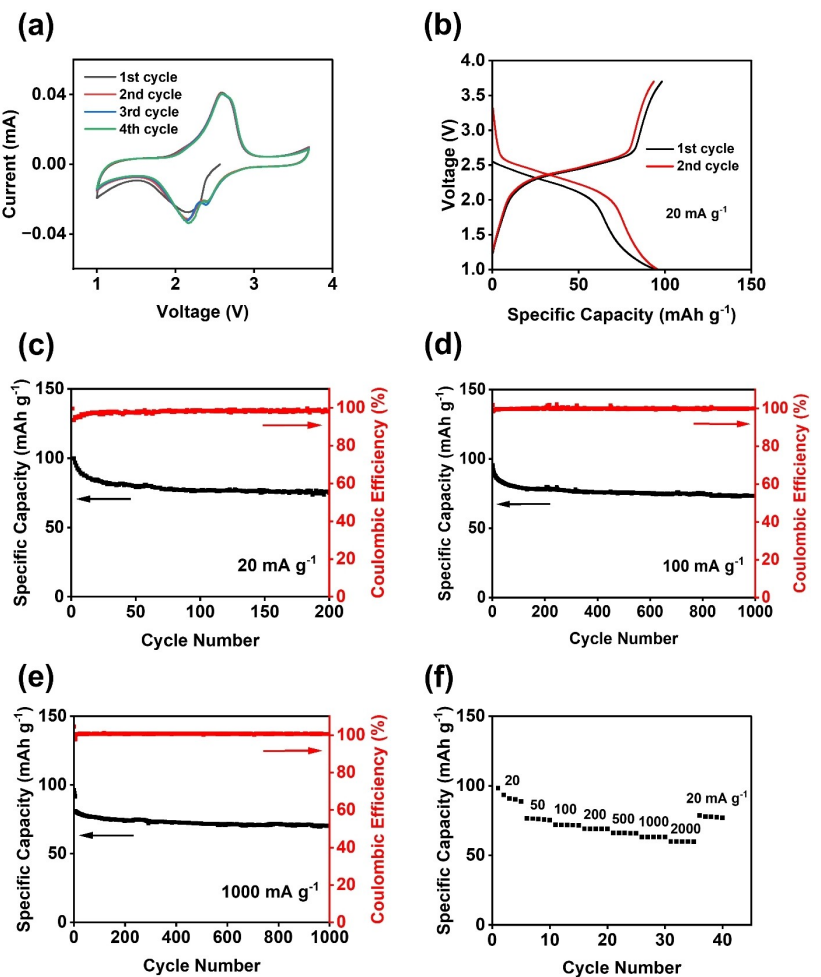


**Figure 7.** Electrochemical performance of PTP in KIBs: a) cyclic voltammograms at  $0.1 \text{ mVs}^{-1}$ ; b) galvanostatic charge-discharge curves at  $20 \text{ mA g}^{-1}$ ; de-potassiation capacity and Coulombic efficiency versus cycle number at the current density of c)  $20 \text{ mA g}^{-1}$ , d)  $100 \text{ mA g}^{-1}$ , e)  $1000 \text{ mA g}^{-1}$ ; f) rate capability at various scan rates.

## Conclusions

In summary, 3D RAPs with extended conjugation structures were synthesized via a facile condensation polymerization method. With the unique 3D architecture, the PTN and PTP cathodes delivered superior electrochemical performances in both NIBs and KIBs in terms of long cycle life and fast reaction kinetics. Extended conjugation structures in the PTP and single-layer graphene boosted the ion/electron transfer between the redox active sites, further improving the stability and fast charging capability. The PTP cathode demonstrated a very stable cycling performance of 8,000 cycles in NIBs and 1,000 cycles in KIBs. Moreover, high capacity retention was also achieved with elevated current densities from  $20 \text{ mA g}^{-1}$  to  $2000 \text{ mA g}^{-1}$ . This fast reaction kinetics is attributed to the surface reaction controlled behaviors as evidenced by CV under various scan rates. The interphasial structure was studied by XPS, confirming the formation of stable NaF/KF-rich CEI in the cathode. In addition, post-cycling characterizations proved the high morphology and chemical structure stability of the polymer cathode before and after cycling. This work demon-

strates that developing 3D RAPs with extended conjugation structures in the repeating units is a promising strategy for achieving high-performance, affordable, and sustainable NIBs and KIBs.

## Experimental Section

**Materials.** Naphthalenetetracarboxylic dianhydride (> 97%) and tetrakis(4-aminophenyl)methane (> 95%) were purchased from TCI, and they were used as received. Perylenetetracarboxylic dianhydride (98%) was received from Acros Organics. Dimethylformamide (99.8%) was purchased from Sigma-Aldrich and stirred for 24 h with magnesium sulfate to remove any trace of water before using it for synthesis. Propionic acid (> 99%) was purchased from Fisher Scientific. The single-layer graphene was received from ACS materials and carbon black (Super P) with above 99% purity was purchased from Alfa Aesar. The binder solution was prepared using sodium alginate purchased from MP Biomedicals. Electrolyte solvents including ethylene carbonate (> 99%), diethyl carbonate (> 99%), and propylene carbonate (99.7%) were purchased from Sigma Aldrich.

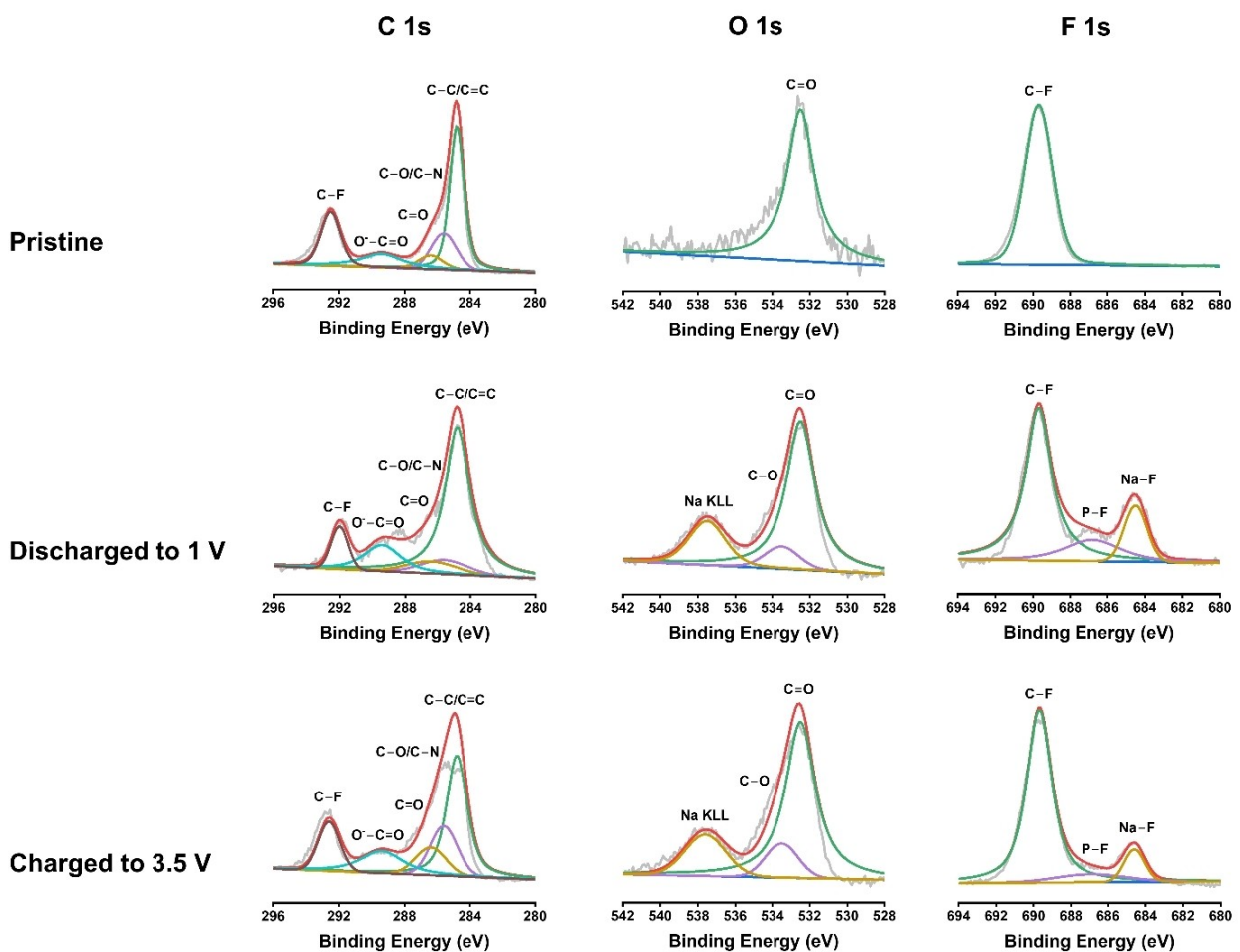


**Figure 8.** XPS spectra of the PTN cathode before and after cycling at the 1–3.5 V window in NIBs. The C 1s, O 1s, and F 1s spectra are displayed in columns, which show the corresponding depth profiling results.

**Polymer synthesis.** PTN was synthesized by a one-pot polycondensation reaction mainly following a reported procedure.<sup>[58]</sup> Naphthalenetetracarboxylic dianhydride (0.8 mmol) was dissolved in 30 mL of Dimethylformamide (DMF) in a 100 mL three-necked flask under refluxing and degassing in a 170 °C oil bath. Tetrakis(4-aminophenyl)methane (0.4 mmol) was dissolved in 10 mL of DMF and added dropwise to the solution. To induce the process, 10 mL of propionic acid was added to the mixture, and stirring continued under a nitrogen atmosphere for 20 hours. The precipitations were collected by centrifuge and washed with tetrahydrofuran, methanol, acetone, and dichloromethane, respectively. The obtained fluffy powders were dried at 100 °C in a vacuum oven overnight.

PTP was also synthesized by a one-pot polymerization according to a literature procedure.<sup>[59]</sup> Perylenetetracarboxylic dianhydride (0.3 mmol) was added to 50 g imidazole and stirred at 150 °C under nitrogen until the imidazole chunks were melted and dissolved the dianhydride. Tetrakis(4-aminophenyl)methane (0.15 mmol) in 10 mL DMF was added drop by drop to the above solution. The mixture was stirred in a 170 °C oil bath for 20 h. After completion of the reaction, the flask was cooled down to 100 °C, and 100 mL of methanol was added. The precipitate was collected by filtration and was washed with DMF and ethanol subsequently. The resulting powder was also washed with tetrahydrofuran, methanol, acetone, and dichloromethane.

**Characterization.** X-ray diffraction (XRD) pattern was recorded by Rigaku MiniFlex using CuK $\alpha$  radiation; Solid-state magic-angle spinning (MAS) NMR experiments were run on a Bruker Avance NEO solid-state 500 MHz NMR spectrometer with a double resonance H/F-X probe: cross-polarization (CP) and magic-angle spinning was used for collecting  $^{13}\text{C}$  and  $^{17}\text{O}$  NMR spectra were obtained by direct observation with MAS. Briefly, samples were packed in a 3.2 mm outer diameter zirconia rotor with Kel-F endcap spinning at 10 kHz for  $^{13}\text{C}$  and  $^{17}\text{O}$ . Proton-carbon matched cross polarization ramp was at 50 kHz with 2 ms contact time. The proton dipolar decoupling was achieved by applying continuous wave spinal64 on the  $^1\text{H}$  channel during acquisition. The  $\pi/2$  pulse length was 2.5  $\mu\text{s}$  for  $^1\text{H}$  and the recycle delay was 4 s. Each  $^{13}\text{C}$  spectrum was collected with 2048 scans and the line broadening for the spectrum was 50 Hz. Each  $^{17}\text{O}$  spectrum was collected from 184320 to 327680 scans with a recycle delay of 0.5 s and the line broadening for the spectrum was 100 Hz.  $^{13}\text{C}$  chemical shifts were referenced with respect to TMS by setting  $\delta(^{13}\text{C}) = 0$  ppm, and  $^{17}\text{O}$  chemical shifts were referenced with respect to water by setting  $\delta(^{17}\text{O}) = 0$  ppm. Fourier-transform infrared spectroscopy (FTIR) was recorded by Agilent Cary 630 FTIR Spectrometer; X-ray photoelectron spectroscopy (XPS) measurements were carried out at a PHI 5000 VersaProbe II system (Physical Electronics) spectrometer, which is equipped with a hemispherical analyzer. The spectrometer is attached to the Ar glovebox and sample transfer was directly through it to avoid any contact of the samples with air and moisture. The spectrometer is attached to the Ar glovebox and

sample transfer was directly through it to avoid any contact of the samples with air and moisture. Monochromatic Al-K $\alpha$  excitation ( $\hbar\nu = 1486.6$  eV) was used at a power of 25 W, additionally applying a low-energy electron charge neutralizer. The high-resolution spectrum of each element was collected with a pass energy of 23.25 eV in an analysis area of  $100 \times 100 \mu\text{m}$ . The binding energy scale was corrected based on the C1s peak from contaminations (C–C at 284.8 eV) as the internal binding energy standard. Scanning electron microscopy (SEM) images were taken by JEOL JSM-IT500HR; The Brunauer-Emmett-Teller (BET) measurements were performed by Micromeritics ASAP 2020 Plus.

**Electrochemical measurements.** The polymeric cathodes were fabricated with PTN/PTP, single-layer graphene, CB, and SA in the ratio of 6:2:1:1. The electrodes were prepared by casting the slurry onto aluminum foil using a doctor blade and dried in a vacuum oven at  $100^\circ\text{C}$  overnight. The dried film was punched into circular electrodes with an average mass loading of  $1.9 \text{ mg cm}^{-2}$ . For the XPS and post-cycling analyses, PTN was mixed with CB and polytetrafluoroethylene (PTFE) in a ratio of 6:3:1 to form high-mass-loading electrodes. The coin cells for Na-ion half cells were assembled using sodium metal as the counter electrode, 1 M NaPF<sub>6</sub> in a mixture of ethylene carbonate (EC): propylene carbonate (PC)/diethyl carbonate (DEC) with a ratio of 1:1 (vol.%) as the electrolytes, and glass fiber (Whatman) as the separator. The K-ion cells were assembled using potassium metal as the counter electrode, 1 M KPF<sub>6</sub> in EC:PC, and glass fiber as the separator. The electrochemical performance was tested using an Arbin battery test station. Cyclic voltammograms were recorded by Gamry Reference 1010E Potentiostat/Galvanostat/ZRA with a scan rate of 0.1–1.0 mV s<sup>-1</sup>. Impedance analysis was also performed by Gamry Reference 1010E Potentiostat/Galvanostat/ZRA.

The theoretical capacity has been calculated using the equation below, where n is the number of electrons participating in the redox reaction, F is the Faraday constant, and M is the molecular weight of the repeating unit of polymers:

$$C_{\text{th}} = \frac{n \times F}{M}$$

Based on the reaction mechanism, both PTN and PTP polymers undergo a four-electron reaction in the repeating units in Scheme 1(a); thus, n is 4. The theoretical capacities for PTN and PTP are 136.04 mAh g<sup>-1</sup> and 103.47 mAh g<sup>-1</sup>, respectively.

**Computational method.** Density functional theory (DFT) calculations were performed using the B3LYP/6-31g(d,p) level of theory with Gaussian 16 to analyze the potential energy surface governing the interactions between benzene and naphthalene diimide (DNI)/perylene-tetracarboxylic diimide (PDI) within the PTN and PTP polymers. Additionally, optimizations of the larger repeating unit were conducted using the GFN2-xTB method.<sup>[79]</sup> The classical molecular dynamics (MD) simulations were performed in GROMACS version 2022<sup>[80]</sup> with OPLS-AA force field.<sup>[81,82]</sup> The repeating unit was stochastically elongated in all spatial dimensions, yielding a monomeric chain comprising approximately 2000 atoms using a custom Python code. Then, 150 single chains were inserted into a 35 nm × 35 nm × 35 nm box to make the polymer system. For each system, an initial energy minimization at 0 K was first performed to obtain the ground-state structure and remove all overlaps. Then, a multi-step compression and relaxation simulation approach introduced by Larsen and Callaway et al<sup>[83,84]</sup> was used to compress the polymer system to a condensed phase.

## Author Contributions

Motahareh Mohammadirodbari: Investigation, Validation, Visualization, Methodology, Writing – original draft; Dr. Shi Li: Validation, Methodology; Jinghao Huang: Validation, Methodology; Dr. Zhenzhen Yang: Methodology, Writing – review & editing; Dr. Fu Chen: Methodology, Writing – review & editing; Dr. Lei Cheng: Methodology, Writing – review & editing; Dr. Chao Luo: Conceptualization, Supervision, Funding acquisition, Project administration, Writing – review & editing.

## Acknowledgements

This work was supported by the US National Science Foundation Award No. 2142003. The authors also acknowledge the support from the George Mason University Quantum Science & Engineering Center. We gratefully acknowledge support from the Post Test Facility at Argonne National Laboratory, which is operated for the DOE Vehicle Technologies Office (VTO) by UChicago Argonne, LLC, under contract number DE-AC02-06CH11357. We thank the NSF (NSF-1726058) for funding a solid-state NMR spectrometer. Ms. Kaitlyn Vi-khanh Ta is acknowledged for technical assistance.

## Conflict of Interests

The authors declare no conflict of interest.

## Data Availability Statement

The data that support the findings of this study are available from the corresponding author upon reasonable request.

**Keywords:** Na-ion batteries • K-ion batteries • redox-active polymers • cathodes • fast-charging batteries

- [1] B. Scrosati, J. Hassoun, Y. K. Sun, *Energy Environ. Sci.* **2011**, *4*, 3287.
- [2] T. Kim, W. Song, D. Y. Son, L. K. Ono, Y. Qi, *J. Mater. Chem. A* **2019**, *7*, 29427.
- [3] J. Xie, Y. C. Lu, *Nat. Commun.* **2020**, *11*, 2499.
- [4] M. Li, J. Lu, Z. Chen, K. Amine, *Adv. Mater.* **2018**, *30*, 1800561.
- [5] J. B. Goodenough, K. S. Park, *J. Am. Chem. Soc.* **2013**, *135*, 1167.
- [6] D. Deng, *Energy Sci. Eng.* **2015**, *3*, 385.
- [7] L. S. Martins, L. F. Guimarães, A. B. Botelho Junior, J. A. S. Tenório, D. C. R. Espinosa, *J. Environ. Manage.* **2021**, *295*, 113091.
- [8] Y. Liu, Y. Zhu, Y. Cui, *Nat. Energy* **2019**, *4*, 540.
- [9] H. Li, X. Zhang, Z. Zhao, Z. Hu, X. Liu, G. Yu, *Energy Storage Mater.* **2020**, *26*, 83.
- [10] T. Perveen, M. Siddiq, N. Shahzad, R. Ihsan, A. Ahmad, M. Imran, *Renewable Sustainable Energy Rev.* **2020**, *119*, 109549.
- [11] P. K. Nayak, L. Yang, W. Brehm, P. Adelhelm, *Angew. Chem. Int. Ed.* **2018**, *57*, 102.
- [12] S. Dhir, S. Wheeler, I. Capone, M. Pasta, *Chem* **2020**, *6*, 2442.
- [13] M. Zhou, P. Bai, X. Ji, J. Yang, C. Wang, Y. Xu, *Adv. Mater.* **2021**, *33*, 2003741.
- [14] T. Hosaka, K. Kubota, A. S. Hameed, S. Komaba, *Chem. Rev.* **2020**, *120*, 6358.

- [15] Y. Liu, C. Gao, L. Dai, Q. Deng, L. Wang, J. Luo, S. Liu, N. Hu, *Small* **2020**, *16*, 2004096.
- [16] A. Auger, C. M. Julien, *Materials* **2020**, *13*, 3453.
- [17] R. Rajagopalan, Y. Tang, C. Jia, X. Ji, H. Wang, *Energy Environ. Sci.* **2020**, *13*, 1568.
- [18] E. J. Kim, P. R. Kumar, Z. T. Gossage, K. Kubota, T. Hosaka, R. Tatara, S. Komaba, *Chem. Sci.* **2022**, *13*, 6121.
- [19] X. Yin, S. Sarkar, S. Shi, Q. A. Huang, H. Zhao, L. Yan, Y. Zhao, J. Zhang, *Adv. Funct. Mater.* **2020**, *30*, 1908445.
- [20] Y. Chen, W. Luo, M. Carter, L. Zhou, J. Dai, K. Fu, S. Lacey, T. Li, J. Wan, X. Han, Y. Bao, L. Hu, *Nano Energy* **2015**, *18*, 205.
- [21] A. Vlad, J. Chen, Y. Yao, *Batteries & Supercaps* **2023**, e202300090.
- [22] R. Thangavel, M. Moorthy, B. K. Ganeshan, W. Lee, W. S. Yoon, Y. S. Lee, *Small* **2020**, *16*, 2003688.
- [23] K. Holguin, K. Qin, E. P. Kamphaus, F. Chen, L. Cheng, G. L. Xu, K. Amine, C. Luo, *J. Power Sources* **2022**, *533*, 231383.
- [24] Y. Lu, J. Chen, *Nat. Chem. Rev.* **2020**, *4*, 127.
- [25] J. Huang, K. I.E. Callender, K. Qin, M. Girgis, M. Paige, Z. Yang, A. Z. Clayborne, C. Luo, *ACS Appl. Mater. Interfaces* **2022**, *14*, 40784.
- [26] B. Esser, F. Dolhem, M. Becuwe, P. Poizot, A. Vlad, D. Brandell, *J. Power Sources* **2021**, *482*, 228814.
- [27] J. J. Shea, C. Luo, *ACS Appl. Mater. Interfaces* **2020**, *12*, 5361.
- [28] K. Holguin, M. Mohammadirooubari, K. Qin, C. Luo, *J. Mater. Chem. A* **2021**, *9*, 19083.
- [29] W. Zhang, J. Yin, W. Wang, Z. Bayhan, H. N. Alshareef, *Nano Energy* **2021**, *83*, 105792.
- [30] S. Muench, A. Wild, C. Fribe, B. Häupler, T. Janoschka, U. S. Schubert, *Chem. Rev.* **2016**, *116*, 9438.
- [31] X. Cao, J. Liu, L. Zhu, L. Xie, *Energy Technol.* **2019**, *7*, 1800759.
- [32] W. Du, X. Du, M. Ma, S. Huang, X. Sun, L. Xiong, *Adv. Funct. Mater.* **2022**, *32*, 2110871.
- [33] J. Kim, J. H. Kim, K. Ariga, *Joule* **2017**, *1*, 739.
- [34] A. Ramar, *J. Mater. Sci. Mater. Electron.* **2020**, *31*, 21832.
- [35] M. Mao, C. Luo, T. P. Pollard, S. Hou, T. Gao, X. Fan, C. Cui, J. Yue, Y. Tong, G. Yang, T. Deng, M. Zhang, J. Ma, L. Suo, O. Borodin, C. Wang, *Angew. Chem., Int. Ed.* **2019**, *58*, 17820.
- [36] R. R. Kapaev, I. S. Zhidkov, E. Z. Kurmaev, K. J. Stevenson, P. A. Troshin, *J. Mater. Chem. A* **2019**, *7*, 22596.
- [37] Y. Chen, S. Zhuo, Z. Li, C. Wang, *EnergyChem* **2020**, 2,100030.
- [38] J. Xie, P. Gu, Q. Zhang, *ACS Energy Lett.* **2017**, *2*, 1985.
- [39] N. Goujon, N. Casado, N. Patil, R. Marcilla, D. Mecerreyes, *Prog. Polym. Sci.* **2021**, *122*, 101449.
- [40] J. Yang, Y. Shi, P. Sun, P. Xiong, Y. Xu, *ACS Appl. Mater. Interfaces* **2019**, *11*, 42305.
- [41] Q. Li, D. Li, H. Wang, H. G. Wang, Y. Li, Z. Si, Q. Duan, *ACS Appl. Mater. Interfaces* **2019**, *11*, 28801.
- [42] I. Gomez, O. Leonet, J. Alberto Blazquez, H. J. Grande, D. Mecerreyes, *ACS Macro Lett.* **2018**, *7*, 419.
- [43] J. Li, M. Luo, Z. Ba, Z. Wang, L. Chen, Y. Li, M. Li, H. B. Li, J. Dong, X. Zhao, Q. Zhang, *J. Mater. Chem. A* **2019**, *7*, 19112.
- [44] M. Ruby Raj, R. V. Mangalaraja, G. Lee, D. Contreras, K. Zaghib, M. V. Reddy, *ACS Appl. Energ. Mater.* **2020**, *3*, 6511.
- [45] H. Wang, H. Wang, H. Wang, C. J. Yao, H. J. Nie, K. Z. Wang, Y. W. Zhong, P. Chen, S. Mei, Q. Zhang, Q. Zhang, *J. Mater. Chem. A* **2020**, *8*, 11906.
- [46] H. Li, M. Tang, Y. Wu, Y. Chen, S. Zhu, B. Wang, C. Jiang, E. Wang, C. Wang, *J. Phys. Chem. Lett.* **2018**, *9*, 3205.
- [47] A. Molina, N. Patil, E. Ventosa, M. Liras, J. Palma, R. Marcilla, *ACS Energy Lett.* **2020**, *5*, 2945.
- [48] M. Wu, Y. Zhao, B. Sun, Z. Sun, C. Li, Y. Han, L. Xu, Z. Ge, Y. Ren, M. Zhang, Q. Zhang, Y. Lu, W. Wang, Y. Ma, Y. Chen, *Nano Energy* **2020**, *70*, 104498.
- [49] S. Gu, Y. Chen, R. Hao, J. Zhou, I. Hussain, N. Qin, M. Li, J. Chen, Z. Wang, W. Zheng, Q. Gan, Z. Li, H. Guo, Y. Li, K. Zhang, Z. Lu, *Chem. Commun.* **2021**, *57*, 7810.
- [50] M. Mohammadirooubari, J. Huang, E. Y. Kim, Z. Yang, F. Chen, C. Luo, *J. Mater. Chem. A* **2023**, *11*, 16636.
- [51] C. Luo, *Chem. Commun.* **2023**, *59*, 9803.
- [52] C. Cui, X. Ji, P. F. Wang, G. L. Xu, L. Chen, J. Chen, H. Kim, Y. Ren, F. Chen, C. Yang, X. Fan, C. Luo, K. Amine, C. Wang, *ACS Energy Lett.* **2020**, *5*, 224.
- [53] C. Peng, G. H. Ning, J. Su, G. Zhong, W. Tang, B. Tian, C. Su, D. Yu, L. Zu, J. Yang, M. F. Ng, Y. S. Hu, Y. Yang, M. Armand, K. P. Loh, *Nat. Energy* **2017**, *2*, 17074.
- [54] M. Mohammadirooubari, K. Qin, C. Luo, *Batteries & Supercaps* **2022**, *5*, e202200021.
- [55] H. Xu, H. Chen, C. Gao, *ACS Materials Lett.* **2021**, *3*, 1221.
- [56] Y. Huang, K. Li, J. Liu, X. Zhong, X. Duan, I. Shakir, Y. Xu, *J. Mater. Chem. A* **2017**, *5*, 2710.
- [57] A. K. Thakur, M. S. Ahmed, G. Oh, H. Kang, Y. Jeong, R. Prabakaran, M. P. Vikram, S. W. Sharshir, J. Kim, J. Y. Hwang, *J. Mater. Chem. A* **2021**, *9*, 2628.
- [58] D. Tian, H. Z. Zhang, D. S. Zhang, Z. Chang, J. Han, X. P. Gao, X. H. Bu, *RSC Adv.* **2014**, *4*, 7506.
- [59] M. R. Raj, N. Kim, G. Lee, *Sustain. Energy Fuels* **2021**, *5*, 175.
- [60] E. R. Andrew, A. Bradbury, R. G. Eades, *Nature* **1958**, *182*, 4650.
- [61] J. C. C. Freitas, D. F. Cipriano, C. G. Zucolotto, A. G. Cunha, F. G. Emmerich, *J. Spectrosc.* **2016**, *2016*, 1543273.
- [62] P. Duan, X. Li, T. Wang, B. Chen, S. J. Juhl, D. Koepfinger, V. H. Crespi, J. V. Badding, K. Schmidt-Rohr, *J. Am. Chem. Soc.* **2018**, *140*, 7658.
- [63] Y. Yesiltepe, J. R. Nuñez, S. M. Colby, D. G. Thomas, M. I. Borkum, P. N. Reardon, N. M. Washton, T. O. Metz, J. G. Teeguarden, N. Govind, R. S. Renslow, *J. Cheminf.* **2018**, *10*, 52.
- [64] I. J. Lowe, *Phys. Rev. Lett.* **1959**, *2*, 285.
- [65] M. Wang, X. P. Wu, S. Zheng, L. Zhao, L. Li, L. Shen, Y. Gao, N. Xue, X. Guo, W. Huang, Z. Gan, F. Blanc, Z. Yu, X. Ke, W. Ding, X. Q. Gong, C. P. Grey, L. Peng, *Sci. Adv.* **2015**, *1*, e1400133.
- [66] B. Tian, G. H. Ning, W. Tang, C. Peng, D. Yu, Z. Chen, Y. Xiao, C. Su, K. P. Loh, *Mater. Horiz.* **2016**, *3*, 429.
- [67] E. Korin, N. Froumin, S. Cohen, *ACS Biomater. Sci. Eng.* **2017**, *3*, 882.
- [68] J. Zheng, S. Chen, W. Zhao, J. Song, M. H. Engelhard, J. G. Zhang, *ACS Energy Lett.* **2018**, *3*, 315.
- [69] Y. Jin, Y. Xu, P. M. L. Le, T. D. Vo, Q. Zhou, X. Qi, M. H. Engelhard, B. E. Matthews, H. Jia, Z. Nie, C. Niu, C. Wang, Y. Hu, H. Pan, J. G. Zhang, *ACS Energy Lett.* **2020**, *5*, 3212.
- [70] X. Yi, A. M. Rao, J. Zhou, B. Lu, *Nano-Micro Lett.* **2023**, *15*, 200.
- [71] Y. Zhang, X. Yi, H. Fu, X. Wang, C. Gao, J. Zhou, A. M. Rao, B. Lu, *small struct.* **2023**, 2300232.
- [72] Z. Li, H. Y. Zhou, F. L. Zhao, T. X. Wang, X. Ding, B. H. Han, W. Feng, *Chin. J. Polym. Sci.* **2020**, *38*, 550.
- [73] H. Dong, H. Gao, J. Geng, X. Hou, S. Gao, S. Wang, S. Chou, *J. Phys. Chem. C* **2021**, *125*, 20814.
- [74] T. B. Schon, A. J. Tilley, E. L. Kynaston, D. S. Seferos, *ACS Appl. Mater. Interfaces* **2017**, *9*, 15631.
- [75] R. Blume, D. Rosenthal, J. P. Tessonnier, H. Li, A. Knop-Gericke, R. Schlögl, *ChemCatChem* **2015**, *7*, 2871.
- [76] A. J. Plomp, D. S. Su, K. P. D. Jong, J. H. Bitter, *J. Phys. Chem. C* **2009**, *113*, 9865.
- [77] S. Peng, S. Yan, N. Wang, W. Nan, J. Wang, X. Chen, C. Wang, X. Qi, S. Dai, *RSC Adv.* **2018**, *8*, 12701.
- [78] B. Tian, J. Zheng, C. Zhao, C. Liu, C. Su, W. Tang, X. Li, G. H. Ning, *J. Mater. Chem. A* **2019**, *7*, 9997.
- [79] C. Bannwarth, S. Ehlert, S. Grimme, *J. Chem. Theory Comput.* **2019**, *15*, 1652.
- [80] H. J. C. Berendsen, D. van der Spoel, R. van Drunen, *Comput. Phys. Commun.* **1995**, *91*, 43.
- [81] W. L. Jorgensen, D. S. Maxwell, J. Tirado-Rives, *J. Am. Chem. Soc.* **1996**, *118*, 11225.
- [82] C. E. S. Bernardes, A. Joseph, *J. Phys. Chem. A* **2015**, *119*, 3023.
- [83] D. Hofmann, L. Fritz, J. Ulbrich, C. Schepers, M. Böhning, *Macromol. Theory Simul.* **2000**, *9*, 293.
- [84] C. P. Callaway, J. H. Bombile, W. Mask, S. M. Ryno, C. Risko, *J. Polym. Sci.* **2022**, *60*, 559.

Manuscript received: October 12, 2023

Revised manuscript received: November 12, 2023

Accepted manuscript online: November 22, 2023

Version of record online: December 8, 2023